RSC Advances

ROYAL SOCIETY
OF CHEMISTRY

PAPER

View Article Online
View Journal | View Issue

Check for updates

Cite this: *RSC Adv.*, 2021, **11**, 15416

Co_9S_8@carbon nanofiber as the high-performance anode for potassium-ion storage†

Wen Xin, Zhixuan Wei, Shiyu Yao, Nan Chen, Chunzhong Wang, Gang Chen and Fei Du *

Received 8th February 2021
Accepted 12th April 2021

DOI: 10.1039/d1ra01069g

rsc.li/rsc-advances

Thanks to their intrinsic merits of low cost and natural abundance, potassium-ion batteries have drawn intense interest and are regarded as a possible replacement for lithium-ion batteries. The larger radius of potassium, however, provides slow mobility, which normally leads to sluggish diffusion of host materials and eventual expansion of volume, typically resulting in electrode failure. To address these issues, we design and synthesize an effective micro-structure with Co_9S_8 nanoparticles segregated in carbon fiber utilizing a concise electrospinning process. The anode delivers a high K^+ storage capacity of 721 mA h g^{-1} at 0.1 A g^{-1} and a remarkable rate performance of 360 mA h g^{-1} at a high current density of 3 A g^{-1}. A small charge-transfer resistance and a high pseudocapacitive contribution that benefit fast potassium ion migration are indicated by quantitative analysis. The outstanding electrochemical performance can be attributed to the distinct architecture design facilitating high active electrode–electrolyte area and fast kinetics as well as controlled volume expansion.

Introduction

The accelerated production of alternative energy sources has been encouraged recently by the decline of non-renewable conventional fossil fuels and increasing environmental issues regarding global warming. So, the development of renewable and effective energy storage systems is inevitable and critical to address the intrinsic erratic properties of solar and wind power.[1–3] Lithium-ion batteries (LIBs) have increasingly gained interest over the past three decades among the possible alternatives. Nevertheless, the shortage and uniform distribution of lithium supplies will eventually increase the cost of LIBs. In comparison with lithium, potassium demonstrates great advantages including the natural abundance (2.09 wt% for potassium *vs.* 0.0017 wt% for lithium), low cost and close redox potential to that of Li^+/Li.[4–6] Hence, potassium-ion batteries (PIBs) are perceived to be a satisfactory alternative for LIB technology.

Among potential anode materials for K^+ storage, transition metal sulfides (TMSs) are popularly investigated because of their multiple electrons reactions which lead to high theoretical capacity.[7–10] In addition, the weaker K–S bond during the conversion reaction is responsible for a more kinetically advantageous redox process.[11] However, the rapid fading of capability, slow kinetics induced by frequent changes in volume and low conductivity are still the key bottlenecks that seriously hinder the feasibility of TMSs in KIBs.[12] Therefore, these concerns need to be overcame to improve the electrochemical performance of TMSs in KIBs.

Nanostructure design, which endows with enhanced inter facial interaction by owning high accessible surface area, shortening ion diffusion pathway and good buffing of mechanical breakdown, are supposed to increase the stability of cycling.[13–15] In particular, one-dimensional (1D) nanostructures can effectively delay the axial mechanical stress of the electrodes caused by volume expansion during cycling. Among the considerable advancements made in the utilization of a safe and controllable process for the preparation of 1D nanostructure composites, due to its unequalled operational simplicity and accessible industrial efficiency production,[16,17] the electrospinning technique is an efficient, innovative and potential approach to the establishment of TMS electrodes.[18–20] For instance, Zhu *et al.*[21] prepared FeS_2@carbon fiber electrode as cathode of rechargeable lithium batteries with superior cycling performance and high discharge energy densities. Chen *et al.*[22] prepared a $SnSbS_x$/porous carbon nanofiber composite *via* electrospinning and demonstrated high performance in sodium-ion batteries. Hu *et al.*[23] established a binder-free and self-standing Co_9S_8@CNT–CNF electrode as cathode for aluminum-ion batteries which show high discharge capacity, enhanced rate performance and extraordinary cycling stability.

Herein, we successfully synthesized 1D Co_9S_8@carbon nanofiber through a facile electrospinning process. The electrospun Co_9S_8 exhibits exceptional potassium storage in terms of reversible specific capacity of 721 mA h g^{-1} at 0.1 A g^{-1},

---

Key Laboratory of Physics and Technology for Advanced Batteries (Ministry of Education), State Key Laboratory of Superhard Materials, College of Physics, Jilin University, Changchun, 130012, China

† Electronic supplementary information (ESI) available. See DOI: 10.1039/d1ra01069g

superior rate capability with specific capacity of 359.7 mA h g^{-1} at 3 A g^{-1} and long cycling stability with capacity retention of 270.6 mA h g^{-1} over 400 cycles. Furthermore, quantitative kinetic studies confirms a small charge-transfer resistance and a major dedication of pseudocapacitive potassium storage mechanism that promotes quick charge transfer. All these observations indicate that it is possible to accept Co_9S_8@carbon nanofiber as a potential high-performance anode for PIBs.

Experimental

Material preparation

The composite nanofibers of $Co(Ac)_2$@PAN were prepared by electrospinning. 1.25 g $Co(Ac)_2$ and 1.25 g PAN ($M_w = 150\ 000$) were dissolved in 17.5 g *N*,*N*-dimethylformamide (DMF) and stirred for 12 hours to prepare the electrospinning solution. The solution was then sprayed from a 19-gauge stainless steel nozzle and collected by the aluminum foil covered on drum collector with following parameters: 20 cm between the nozzle and the collector, 100 rpm revolving speed of the drum and 25 kV applied voltage during the working process. The resulting $Co(Ac)_2$@PAN composite nanofibers were then stabilized at 220 °C in air for 1 h, then was calcinated under Ar atmosphere at a temperature of 500 °C for 5 h (5 °C min^{-1}), followed by a sulfuration process of calcining at 300 °C (5 °C min^{-1}) under Ar/H_2 atmosphere with excessive S powder. The Co_9S_8 without carbon fiber was prepared in the same condition without the electrospinning with PAN. The pure carbon nanofiber was prepared in the same condition without adding $Co(Ac)_2$ and the sulfuration process.

Materials characterization

A Rigaku D/max-2550 diffractometer with Cu Kα radiation was utilized to collect X-ray diffraction (XRD) characterizations. Microscopic morphologies of Co_9S_8@carbon nanofiber were evaluated by a field emission scanning electron microscope (JEOL JSM-6700F) and TEM (FEI Tecnai G2F20S-TWIN). The thermogravimetric analysis (TGA) was measured by SDT Q600. X-ray photoemission spectrum (XPS) was carried out on a VG scientific ESCALAB-250 spectrometer.

Electrochemical test

The electrospun Co_9S_8@carbon nanofiber was mixed with Super P and sodium carboxymethyl cellulose (CMC) in a mass ratio of 7 : 2 : 1 to prepare the electrodes by pasting the slurry onto a copper foil. The electrode was then clipped into circular discs of 1 cm diameter with a loading mass of 1.0–1.2 mg cm^{-2} after drying at 60 °C for 12 h in vacuum oven. The established anode electrode combining with a counter and reference electrode (sliced potassium metal foil) and a separator (Whatman GF/F glass fiber) were assembled into a CR2032 coin-type cells in an argon-filled glove-box. And the electrolyte was 1.0 m potassium hexafluorophosphate (KPF_6) in 1 : 1 (volume ratio) ethylene carbonate: diethyl carbonate. Land-2100 automatic battery tester was used to test the galvanostatic charge–discharge between 0.01 and 3 V. VSP multichannel potentiostatic–galvanostatic system (Bio-Logic SAS, France) was employed to study electrochemical impedance spectroscopy (EIS) and cyclic voltammetry (CV).

Results and discussion

As shown in Fig. 1a, the Co_9S_8@carbon nanofiber was synthesized using electrospinning techniques, accompanied by processes of thermal treatment and sulfurization. X-ray diffraction (XRD) characterizations was utilized to verify the phase purity and crystal structure of Co_9S_8@carbon nanofiber (Fig. 1b). It is obvious that all diffraction peaks are well aligned with that of cubic-phase Co_9S_8 (PDF#05-0562) without any additional peaks, applying the absence of impurities. To validate the carbon content of the nanocomposite, thermogravimetric analysis (TGA) was conducted in the air. As illustrated in Fig. 1c, a minor weight loss below 200 °C is attributed to unavoidable moisture evaporation owing to atmospheric conditions storage of sample. Due to the formation of Co_3O_4 and $CoSO_4$ responded by Co_9S_8 with O_2 in the air, the augment of weight can be detected between 200 and 400 °C as the temperature increases. $CoSO_4$ then continues to decompose to Co_3O_4 and Co_3O_4 constantly raises. Finally, $CoSO_4$ disappears entirely leaving Co_3O_4 as the final product.[24] The carbon content is calculated to be 62.48%. To further explore the chemical binding states of Co_9S_8@carbon, XPS was carried out, which is consistent with the previous reported results.[24,25] As shown in Fig. S1a,† the high-resolution Co 2p spectrum exhibits two major peaks at 778.5 eV and 793.4 eV, corresponding to Co $2p_{3/2}$ and Co $2p_{1/2}$ of Co^{2+} respectively. While, two peaks come from Co $2p_{3/2}$ and Co $2p_{1/2}$ of Co^{3+} can be observed at 781.4 eV and 797.0 eV. The appearance of Co^{3+} might be due to the surface oxidization in air. S 2p spectrum are also shown in Fig. S1b† with the characteristic peaks of S $2p_{3/2}$ and S $2p_{1/2}$ at 160.75 eV and 163.5 eV. In addition, two peaks at 164.1 eV and 167.65 eV result from S_n^{2-} and S=O.

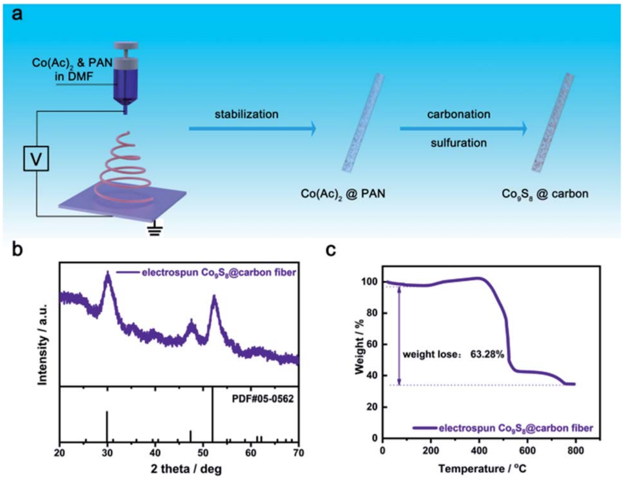

Fig. 1 (a) Schematic of synthesis electrospun Co_9S_8@carbon fiber; (b) the XRD pattern of Co_9S_8@carbon fiber; (c) the TGA curse of Co_9S_8@carbon fiber.

The Co_9S_8@carbon nanofiber architecture was detected by electron microscopy scanning (SEM). The as-prepared materials display a uniform 1D-nanofiber morphology with various diameters varying from 100 to 200 nm, as seen in Fig. 2a–c. Transmission electron microscopy (TEM) was then used to continuing analyze as-prepared fiber's micro-scopic features and inner components. Fig. 2d and e shows an individual Co_9S_8@carbon nanofiber, which clearly shows that the Co_9S_8 particles with dimension of 10–20 nm are harmoniously dispersed in the nanofiber. In the meanwhile, the carbon segregates the Co_9S_8 particles in the nanofiber and can serve as conductive network during the electrochemical reactions. The corresponding selected region electron diffraction (SAED) pattern (Fig. 2f), has further confirmed the well-defined crystallinities of Co_9S_8@carbon nanofiber. And the polycrystalline nature of the Co_9S_8 nanoparticles is verified by several bright diffraction rings that are well aligned with the cubic-phase Co_9S_8, which could be ascribed to the random orientation of the Co_9S_8 particles in the carbon nanofiber.[26] Meanwhile, a distinct interplanar spacing of 0.29 nm index to the (311) cubic-phase plane Co_9S_8 is given by the HRTEM images (inset of Fig. 2e). Besides, the elemental mapping images (Fig. 2g) manifest that in the Co_9S_8@carbon nanofiber composite, Co and S are spread uniformly. Such a hierarchical architecture will benefit from electrolyte penetration, shorten the pathway of ion diffusion, as well as improve the adequate interaction of the active materials and the electrolyte. In particular, the unique structure with the internal nanosized active material and external carbon matrix can buff the pressure induced by volume expansion that improves the cycle performance of electrode.

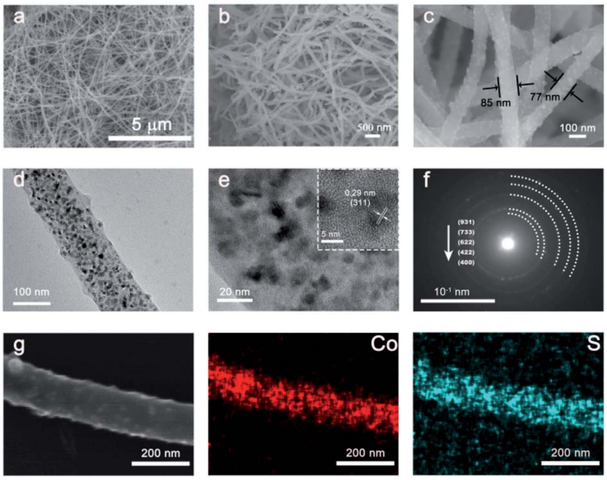

Fig. 2 (a–c) SEM images (d and e) TEM images, (f) selected area electron diffraction (SAED) pattern, (g) element mapping of the as-synthesized Co_9S_8@carbon fiber. The inset of (d) shows the HRTEM image.

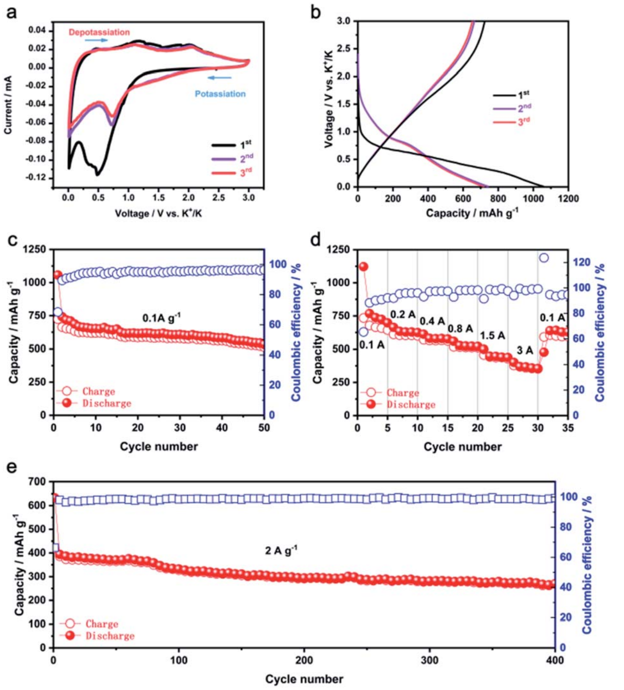

Fig. 3 (a) Cyclic voltammograms (CV) curse at a scanning rate of 0.1 mV s^{-1}; (b) galvanostatic discharge/charge potential profiles of the first three cycles at 0.1 A g^{-1}, (c) cycling performance at 0.1 A g^{-1}; (d) rate performance at different current densities from 0.1 to 3 A g^{-1} and (e) long-term cycling performance at 2 A g^{-1} of Co_9S_8@carbon fiber electrode.

The potassium storage properties of Co_9S_8@carbon nanofiber were valued in a voltage range of 0.01–3 V (*vs.* K^+/K). The Co_9S_8 anode's cyclic voltammograms curves obtained at a scan rate of 0.1 mV s^{-1} are depicted in Fig. 3a. In the cathodic scan of initial cycle, two peaks attributed to the conversion reaction between Co_9S_8 and K to the Co and K_2S matrix and solid electrolyte interphase formation (SEI) were found at 0.47 V and 0.33 V. While three distinct peak at 1.1 V, 1.8 V and 2 V in the anodic scan are ascribed to the conversion reaction between Co and K_2S to stepwise form Co_9S_8, consistent with the previous studies.[24] From the second cycle, only one peak at 0.7 V in the cathodic scan and two peaks at 1.1 V and 2.1 V in the anodic scan ascribed to the reversible conversion reaction between Co_9S_8 and K can be observed. The difference between the first two cycles of redox peaks are related to the activated process of electrode and the irresponsibility of SEI formation in the first cycle. The following curves nearly coincide with each other suggesting the superior reversibility of the redox reaction, except for the remarkable discrepancy between the first two periods. The initial discharge capacity is achieved as 1050 mA h g^{-1} while a capacity of 721 mA h g^{-1} with a coulombic efficiency (CE) of 68.7% is obtained in the charging process because of the nonreciprocal generating of SEI film on the electrode, which is a normal phenomenon in conversion- or alloying-type anodes (Fig. 3b). And the voltage plateaus in the Co_9S_8 potential profiles of the galvanostatic charge–discharge (GCD) align up with the redox positions in the related CV curves. After the fifth cycles, the coulombic efficiency increases to 95%, indicative a good reversibility. In contrast, as shown in Fig. S2a and b,† Co_9S_8 particles exhibits rapid capacity fading with poor coulombic efficiency due to uncontrolled volume expansion. Meanwhile, the pure carbon fiber can only deliver 150 mA h g^{-1}

capacity at a current density of 0.1 A g^{-1}. Considering the content of carbon in the composite electrode, the carbon fiber can only contribute 93 mA h g^{-1}, which indicates the well-engineered architecture not only effectively suppresses the negative effect of volume expansion, but also increase the reversible capacity. As illustrated in Fig. 3c a reversible capacity of 515 mA h g^{-1} may still persist for the Co_9S_8 anode after 50 cycles. Rate performance of the electrospun Co_9S_8 electrodes was evaluated with current densities rising gradually from 0.1 to 3 A g^{-1} (Fig. 3d). The reversible capacities are delivered as 724 (0.1 A g^{-1}), 629 (0.2 A g^{-1}), 579 (0.4 A g^{-1}), 514 (0.8 A g^{-1}) and 438 (1.5 A g^{-1}) mA h g^{-1}, respectively. Even at a high current density of 3 A g^{-1}, a reversible capacity of 359.7 mA h g^{-1} can be generated signifying a superior rate capability. While, both Co_9S_8 particles and pure carbon nanofiber demonstrate poor rate performance at high applied current densities (Fig. S2c and d†). This suggests that the excellent rate performance is boosted by synergistic effect of outer carbon nanofiber and inner small Co_9S_8 particle. Impressively, the rate capability of Co_9S_8@-carbon nanofiber outperforms most of the transition metal sulfide anodes reported for PIBs, as shown in Fig. S3.† As illustrated in Fig. 3e, the long cycle performance of the Co_9S_8 anode was assessed at a current density of 2 A g^{-1}, the electrode exhibits a steady reversible capacity of 265.6 mA h g^{-1}, even after 400 cycles.

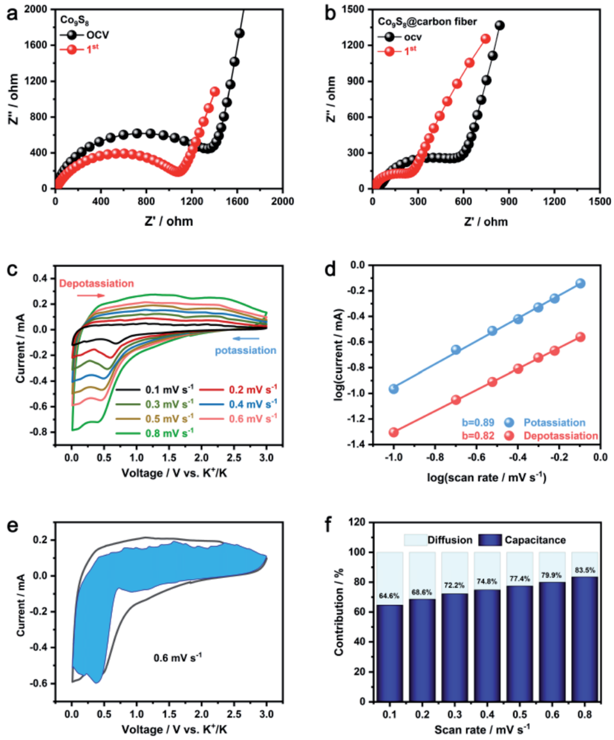

Fig. 4 Nyquist plots of OCV and after first cycle of (a) Co_9S_8 electrodes; (b) electrospun Co_9S_8@carbon fiber electrodes; (c) CV curves of the Co_9S_8 electrode at various scan rates; (d) log(*i*) *versus* log(ν) plots; (e) CV curve with capacitive- and diffusion-controlled contributions at 0.6 mV s^{-1}; (f) the ratio of pseudocapacitive contribution at different scan rates.

Electrochemical impedance spectroscopy (EIS) measurements were utilized to discover the reaction kinetics of electrospun Co_9S_8@carbon fiber to further uncover the potential profile (Fig. 4a and b), consisting of a depressed high-frequency semicircle followed by a sloping straight line in the explanation for the high performance described above. At the OCV and after the first cycles, the Nyquist plots are identical in low-frequency region. The interfacial charge-transfer resistance (R_{ct}) is indicate by the semicircle of high-frequency, whereas a low-frequency slope line is correlated with the Warburg impedance of K-ion diffusion and phase transition within bulk crystals.[27] Apparently, the R_{ct}-value of the as electrospun Co_9S_8@carbon fiber is evidently lower than the R_{ct}-value of pure Co_9S_8. The high ionic diffusivity of Co_9S_8@carbon fiber was attributed to the shortened migration path of electrons and K-ion aided by collaborative architecture of the outer conductive network and small Co_9S_8 particle. For the purpose of understanding the potassium ion storage processes, CV curves at various scan rates were also studied (Fig. 4c). The connection between calculated peak current (*i*) and the corresponding sweep rate (ν) may be defined by the following equation:[28]

$$i = a\nu^b \tag{1}$$

The *b* value can be obtained from the slope of the profile *via* plotting log(*i*) *versus* log(ν), and a *b*-value of 0.5 implies a full diffusion-controlled activity meanwhile a surface-controlled behavior corresponds to a *b*-value of 1 (capacitive process). In the potassiation process, the *b* value are determined to be 0.89 while a *b* values of 0.82 can be calculated for the depotassiation process (Fig. 4d). This means the conversion reaction of Co_9S_8@carbon fiber in PIBs is a mixed processes of diffusion mechanisms and capacitance reaction mechanisms. In addition, quantitative analysis based on the CV data collected at various scanning frequencies typically indicated the pseudocapacitance contribution, by means of the following equation, the combined mechanism can be separated into two distinct sections:

$$i = k_1\nu + k_2\nu^{1/2} \tag{2}$$

where k_1 and k_2 are constants at a given potential. Based on the curve of $i(\nu)/\nu^{1/2}$ *versus* $\nu^{1/2}$, the values of k_1 and k_2 can be computed, and then the ratio of pseudocapacitive contribution at different scan rates were also calculated by the slope and the *y*-axis intercept of the plot (Fig. 4f). As scan rate rise from 0.1 mV s^{-1} to 0.8 mV s^{-1}, a maximum capacitive contribution of 83.5% can be received. We may infer from the above results that pseudocapacitance occupies the main position, especially at high scan rates, in the electrochemical reaction of electrospun Co_9S_8 anode. The collaborative architecture of the outer conductive network and small Co_9S_8 particles, which shortened the transport path and boost the transfer of potassium ion, may be the main cause of such a high capacitance contribution.

Conclusion

On the whole, we use an electrospinning method to prepare the Co_9S_8@carbon nanofiber. The well engineered architecture showed a morphology of 1D nanofiber dispersed with Co_9S_8 particle ranged from 10 to 20 nm uniformly, which can shorten the pathway of ion diffusion as well as buff the volume expansion during conversion reactions with large-sized potassium ions. As a consequence, the electrospun Co_9S_8@carbon nanofiber electrode provides outstanding electrochemical performance in PIBs: a high capacity of 721 mA h g^{-1} at 0.1 A g^{-1} and a capacity of 359.7 mA h g^{-1} at a high current rate of 3 A g^{-1} can be achieved. Quantitative analysis implies that small charge-transfer resistance and high pseudocapacitance content lead to the rapid mechanism of potassium ion storage, which facilitates the PIB rate capability of Co_9S_8. The consequence above suggest that Co_9S_8 may be a potential choice for high performance anode for PIBs.

Conflicts of interest

There are no conflicts to declare.

Acknowledgements

This work was supported by National Natural Science Foundation of China (no. 51972142), Science and Technology Development Project, Jilin Province (grant no. 20180101211JC and 20190701020GH) and the Fundamental Research Funds for the Central Universities.

Notes and references

1 B. Dunn, H. Kamath and J.-M. Tarascon, Electrical energy storage for the grid: a battery of choices, *Science*, 2011, **334**(6058), 928–935.

2 N. Yabuuchi, *et al.*, Research development on sodium-ion batteries, *Chem. Rev.*, 2014, **114**(23), 11636–11682.

3 W. Zhang, Y. Liu and Z. Guo, Approaching high-performance potassium-ion batteries via advanced design strategies and engineering, *Sci. Adv.*, 2019, **5**(5), eaav7412.

4 J. Chen, D. H. Chua and P. S. Lee, The Advances of Metal Sulfides and In Situ Characterization Methods beyond Li Ion Batteries: Sodium, Potassium, and Aluminum Ion Batteries, *Small Methods*, 2020, **4**(1), 1900648.

5 K. Song, *et al.*, Recent Progress on the Alloy-Based Anode for Sodium-Ion Batteries and Potassium-Ion Batteries, *Small*, 2019, 1903194.

6 S. Wang, *et al.*, A Stable Conversion and Alloying Anode for Potassium-Ion Batteries: A Combined Strategy of Encapsulation and Confinement, *Adv. Funct. Mater.*, 2020, 2001588.

7 L. Fang, *et al.*, Few-Layered Tin Sulfide Nanosheets Supported on Reduced Graphene Oxide as a High-Performance Anode for Potassium-Ion Batteries, *Small*, 2019, **15**(10), 1804806.

8 H. Lin, *et al.*, Nanosheets-Assembled CuSe Crystal Pillar as a Stable and High-Power Anode for Sodium-Ion and Potassium-Ion Batteries, *Adv. Energy Mater.*, 2019, **9**(20), 1900323.

9 L. Yang, *et al.*, Hierarchical NiS_2 Modified with Bifunctional Carbon for Enhanced Potassium-Ion Storage, *Adv. Funct. Mater.*, 2019, **29**(50), 1903454.

10 C. Zhang, *et al.*, Improving compactness and reaction kinetics of MoS_2@C anodes by introducing Fe_9S_{10} core for superior volumetric sodium/potassium storage, *Energy Storage Materials*, 2020, **24**, 208–219.

11 Q. Zhou, *et al.*, Co_3S_4@polyaniline nanotubes as high-performance anode materials for sodium ion batteries, *J. Mater. Chem. A*, 2016, **4**(15), 5505–5516.

12 Z. Hu, *et al.*, Advances and challenges in metal sulfides/selenides for next-generation rechargeable sodium-ion batteries, *Adv. Mater.*, 2017, **29**(48), 1700606.

13 H. Tan, *et al.*, Metal Chalcogenides: Paving the Way for High-Performance Sodium/Potassium-Ion Batteries, *Small Methods*, 2020, **4**(1), 1900563.

14 S. Yan, *et al.*, GeO_2 Encapsulated Ge Nanostructure with Enhanced Lithium-Storage Properties, *Adv. Funct. Mater.*, 2019, **29**(8), 1807946.

15 Y. Jiang, *et al.*, Highly reversible Na storage in Na_3V_2 $(PO_4)_3$ by optimizing nanostructure and rational surface engineering, *Adv. Energy Mater.*, 2018, **8**(16), 1800068.

16 J. K. Y. Lee, *et al.*, Polymer-based composites by electrospinning: Preparation & functionalization with nanocarbons, *Prog. Polym. Sci.*, 2018, **86**, 40–84.

17 S. Peng, *et al.*, Multi-functional electrospun nanofibers for advances in tissue regeneration, energy conversion & storage, and water treatment, *Chem. Soc. Rev.*, 2016, **45**(5), 1225–1241.

18 X. Li, *et al.*, Electrospun carbon-based nanostructured electrodes for advanced energy storage–a review, *Energy Storage Materials*, 2016, **5**, 58–92.

19 S. Peng, *et al.*, Electronic and Defective Engineering of Electrospun $CaMnO_3$ Nanotubes for Enhanced Oxygen Electrocatalysis in Rechargeable Zinc–Air Batteries, *Adv. Energy Mater.*, 2018, **8**, 1800612.

20 D. Ji, *et al.*, Atomically Transition Metals on Self-Supported Porous Carbon Flake Arrays as Binder-Free Air Cathode for Wearable Zinc−Air Batteries, *Adv. Mater.*, 2019, **31**, 1808267.

21 Y. Zhu, *et al.*, Electrospun FeS_2@carbon fiber electrode as a high energy density cathode for rechargeable lithium batteries, *ACS Nano*, 2016, **10**(1), 1529–1538.

22 C. Chen, *et al.*, In-situ formation of tin-antimony sulfide in nitrogen-sulfur Co-doped carbon nanofibers as high performance anode materials for sodium-ion batteries, *Carbon*, 2017, **120**, 380–391.

23 Y. Hu, *et al.*, A Binder-Free and Free-Standing Cobalt Sulfide@Carbon Nanotube Cathode Material for Aluminum-Ion Batteries, *Adv. Mater.*, 2018, **30**, 1703824.

24 G. Ma, *et al.*, Carbon-coated mesoporous Co_9S_8 nanoparticles on reduced graphene oxide as a long-life and high-rate anode material for potassium-ion batteries, *Nano Res.*, 2020, 802–809.

25 B. Xie, *et al.*, Pseudocapacitive Co_9S_8/graphene electrode for high-rate hybrid supercapacitors, *Carbon*, 2019, 134–142.

26 Y. Zhou, *et al.*, Hollow nanospheres of mesoporous Co_9S_8 as a high-capacity and long-life anode for advanced lithium ion batteries, *Nano Energy*, 2015, **12**, 528–537.

27 L. Yuan, *et al.*, New insight into the discharge process of sulfur cathode by electrochemical impedance spectroscopy, *J. Power Sources*, 2009, **189**(1), 127–132.

28 J. Wang, *et al.*, Pseudocapacitive contributions to electrochemical energy storage in TiO_2 (anatase) nanoparticles, *J. Phys. Chem. C*, 2007, **111**(40), 14925–14931.